PCCP

PAPER

View Article Online
View Journal | View Issue

Cite this: *Phys. Chem. Chem. Phys.*, 2025, **27**, 16842

Unlocking a near 1 eV direct band gap, lattice-matched InN–As heterostructure with moist resistance for enhanced optoelectronic applications†

Yee Hui Robin Chang, *[a] Keat Hoe Yeoh, *[b] Junke Jiang, ‡[c] Moi Hua Tuh*[d] and Qiuhua Liang[e]

Received 14th June 2025,
Accepted 17th July 2025

DOI: 10.1039/d5cp02275d

rsc.li/pccp

Hexagonal indium nitride (InN) and arsenene (As) are two examples of experimentally validated two-dimensional (2D) materials that have been regarded promising for use in nanoelectronic devices. However, the current endeavor is centered on manipulating their electronic properties, specifically ways to induce the transition from an indirect to a direct band gap (E_g) in them. To overcome this challenge, we performed first-principles calculations to thoroughly examine the possibility of attaining a direct E_g compound by considering several stacking configurations of InN and As monolayers. The calculated binding energies (E_b) indicate that the stacking configuration with As positioned above In has higher stability compared to other stacking modes. It has a type-II band alignment with a direct E_g of 0.91 eV and a reasonable carrier mobility ($\mu \sim 10^3$ cm^2 V^{-1} s^{-1}), making it highly suited for absorbing visible light. As a result, improved optical absorption intensity and photo response range in the proposed heterostructure are also observed compared with individual InN and As monolayers.

1. Introduction

The discovery of 2D carbon in the structure of a single-layer honeycomb graphene[1] initiated the present extensive investigation into several 2D materials. Nevertheless, the absence of an inherent E_g limits the use of graphene, a characteristic that is also present in graphene-like structures of other group IV elements including silicene (Si), germanene (Ge) and stanene (Sn).[2] A potential solution to this problem is the use of layered materials composed of group V atoms, such as As. According to the theoretical study by Zhao *et al.*,[3] As monolayers can exist in a number of structural phases. The buckled honeycomb structure, planar arrangements and other more intricate reconstructions are examples of these phases, some of which have recently been investigated both theoretically and experimentally. It also emphasizes the necessity of carefully choosing the best phase depending on particular application needs including electronic performance, lattice compatibility and structural stability. In 2019, Shah *et al.*[4] introduced the honey-comb monolayer of As, in which an indirect E_g value of 1.47 eV has been reported, offering a valuable direction for subsequent experimental investigations. On the other hand, Wu *et al.*[5] effectively produced an InN monolayer using the process of molecular beam epitaxy, with reported indirect E_g that varies between 0.70 and 0.80 eV. Following that, Sugita *et al.*[6] reported another successful synthesis of an InN monolayer *via* metalorganic chemical vapour deposition (MOCVD), where a fundamental E_g of approximately 0.70 eV was collectively agreed. Similar to various perovskites and transition metal compounds,[7,8] the indirect E_g in these two monolayers frequently leads to a relatively reduced photoluminescence output and low power conversion efficiency (PCE).

On a brighter note, 2D materials have been shown to possess adjustable bandgaps, which can be obtained by changing the thickness of the layers, manipulating strain, altering chemical bonding, introducing substitutional doping or influencing interface effects *via* heterostructure formation.[9–11] Many

[a] *Faculty of Applied Sciences, Universiti Teknologi MARA, Cawangan Sarawak, 94300 Kota Samarahan, Sarawak, Malaysia. E-mail: robincyh@uitm.edu.my*
[b] *Jeffrey Sachs Center on Sustainable Development, Sunway University, No. 5, Jalan Universiti, Bandar Sunway 47500, Selangor, Malaysia. E-mail: keathoey@sunway.edu.my*
[c] *Materials Simulation and Modelling, Department of Applied Physics, Eindhoven University of Technology, 5612 Eindhoven, The Netherlands*
[d] *Faculty of Computer and Mathematical Sciences, Universiti Teknologi MARA, Cawangan Sarawak, 94300 Kota Samarahan, Sarawak, Malaysia. E-mail: tuhmoihua@uitm.edu.my*
[e] *Department of Physics, Chalmers University of Technology, SE-41296, Gothenburg, Sweden*

† Electronic supplementary information (ESI) available. See DOI: https://doi.org/10.1039/d5cp02275d

‡ Present Address: Univ Rennes, ENSCR, CNRS, ISCR-UMR 6226, F-35000 Rennes, France.

computational studies have conducted screenings and predictions of numerous stable chemicals with a direct E_g suitable for use in solar cells.[12,13] While it is possible to alter electronic properties in individual materials, there are still hurdles to overcome in order to achieve certain additional properties, such as efficient separation of electron–hole pairs and effective suppression of photogenerated carrier recombination. The idea of 2D heterostructures has been suggested as a solution to tackle these difficulties, providing a promising opportunity to investigate novel prospects in photovoltaic research. Currently, the synthesis of van der Waals (vdW) heterostructures is mostly focused on hexagonal 2D structures, as they have a similar structure to graphene. Following this strategy, the indirect E_g limitation in InN and As motivated us to look into the possibility of maximizing the performance of these monolayers through heterostructure formation. In this context, it is worth noting that As has already demonstrated considerable potential for forming vdW heterostructures with various other 2D materials. For instance, heterostructures such as As/$MoSi_2N_4$[14] and As/C_3N[15] have been proposed, exhibiting tunable electronic and optoelectronic properties. These studies reflect the structural compatibility and flexibility of As in heterostructure engineering, further reinforcing its potential as a foundational element for high-performance 2D devices. Inspired by these advances, we investigate the InN/As heterostructure as a potential solution to address the limitations of individual monolayers and improve their collective optoelectronic properties.

We initiated our approach by designing several InN/As stackings, enabling each stacking to relax freely and reach its ground state configuration. We then compared the total energy of each stacking. Thereafter, we evaluated the stability of the selected stacking by conducting a thorough investigation of its phonon spectrum and *ab initio* molecular dynamics (AIMD) simulations. The analyses provided verification of the material's stability. Subsequently, we conducted an analysis of the electronic and optical characteristics, taking into account the influence of many-body interactions. Based on the findings of the electronic and optical properties, we identified a new vdW heterostructure with direct E_g and improved visible light harvesting performance compared to its individual monolayers. The vdW feature is crucial as it enables the distinctive electronic and optical attributes in constituent nanosheets to be retained.

2. Computational methods

The computations herein were performed using the density functional theory (DFT) within the Vienna *Ab Initio* Software Package (VASP) code,[16,17] employing the Perdew–Burke–Ernzerhof (PBE)[18] generalized gradient approximation (GGA) and the projected augmented wave (PAW)[19] approach. The valence states of $4d^{10}5s^25p^1$, $2s^22p^3$ and $3d^{10}4s^24p^3$ were employed for In, N and As, respectively. To account for accurate treatment of long-range vdW interactions, we incorporated the vdW correction Becke–Johnson damping suggested by Grimme (DFT-D3).[20,21] The cutoff energy for the plane-wave basis set was specified at 560 eV. The Brillouin zone was sampled using a Gamma-centered k-point mesh of $7 \times 7 \times 1$ during geometric optimizations, which was subsequently increased to $15 \times 15 \times 1$ for optoelectronic calculations. The convergence thresholds for the electronic self-consistent iteration and force were defined as 10^{-5} eV and 10^{-3} eV Å^{-1}, respectively. A vacuum region of 30 Å thickness was added to reduce the interactions between periodic images.

The thermodynamic stability is assessed through the E_b computation, which was determined by subtracting the total energy of the InN/As heterostructure ($E_{InN/As}$) from that of the isolated monolayers (E_{InN} and E_{As}), as follows.[22–25]

$$E_b = \frac{E_{InN/As} - (E_{InN} + E_{As})}{A}$$

where A denotes the interface area. To determine the optical properties, we utilized the Bethe–Salpeter Equation (BSE) approach, which was integrated with DFT to establish the absorption coefficient, as computed using

$$\alpha(\omega) = \sqrt{2}\omega\left[\sqrt{\varepsilon_1^2(\omega) + \varepsilon_2^2(\omega)} - \varepsilon_1(\omega)\right]^{\frac{1}{2}} \quad (2)$$

where $\varepsilon_1(\omega)$ and $\varepsilon_2(\omega)$ represent the real and imaginary dielectric functions, respectively. The latter can be evaluated by summing-up over empty states while the former is determined by applying Kramers–Kronig transformation involving the $\varepsilon_2(\omega)$ part, as described in ref. 26–28.

3. Results and discussion

3.1. Stability and the electronic properties of the InN–As heterostructure

We initially constructed and examined the lattice constants of the isolated monolayers. Fig. 1(a) and (b) depict the atomic structure of the monolayers. The lattice constants of the optimized InN and As monolayers are $a = b = 3.57$ Å and $a = b = 3.61$ Å, respectively, which align with prior research findings.[22,29] Fig. 1(c) and (d) demonstrate that both InN and As have non-coinciding valence band maximum (VBM) and conduction band minimum (CBM) according to the PBE calculations, indicating indirect E_g that measures 0.62 and 1.64 eV, respectively. The observed band types and E_g sizes of both monolayers are in accordance with the findings reported in earlier experimental research,[4–6] further confirming the accuracy as well as reliability of our results. Since the E_g of the monolayers in the PBE model closely approximates those of experimental measurements, we thereby employed the PBE method to perform all the computations. The InN/As heterostructure was formed by stacking a 2×2 InN unit cell with a 2×2 As unit cell along the z-axis, taking advantage of their extremely close lattice constants. The InN/As superlattice exhibits an impressively small lattice mismatch of 1.1%, significantly below the commonly applied criterion of 5%, which suggests a favorable heterostructure and allows for the practical implementation of the InN/As heterostructure in experiments.

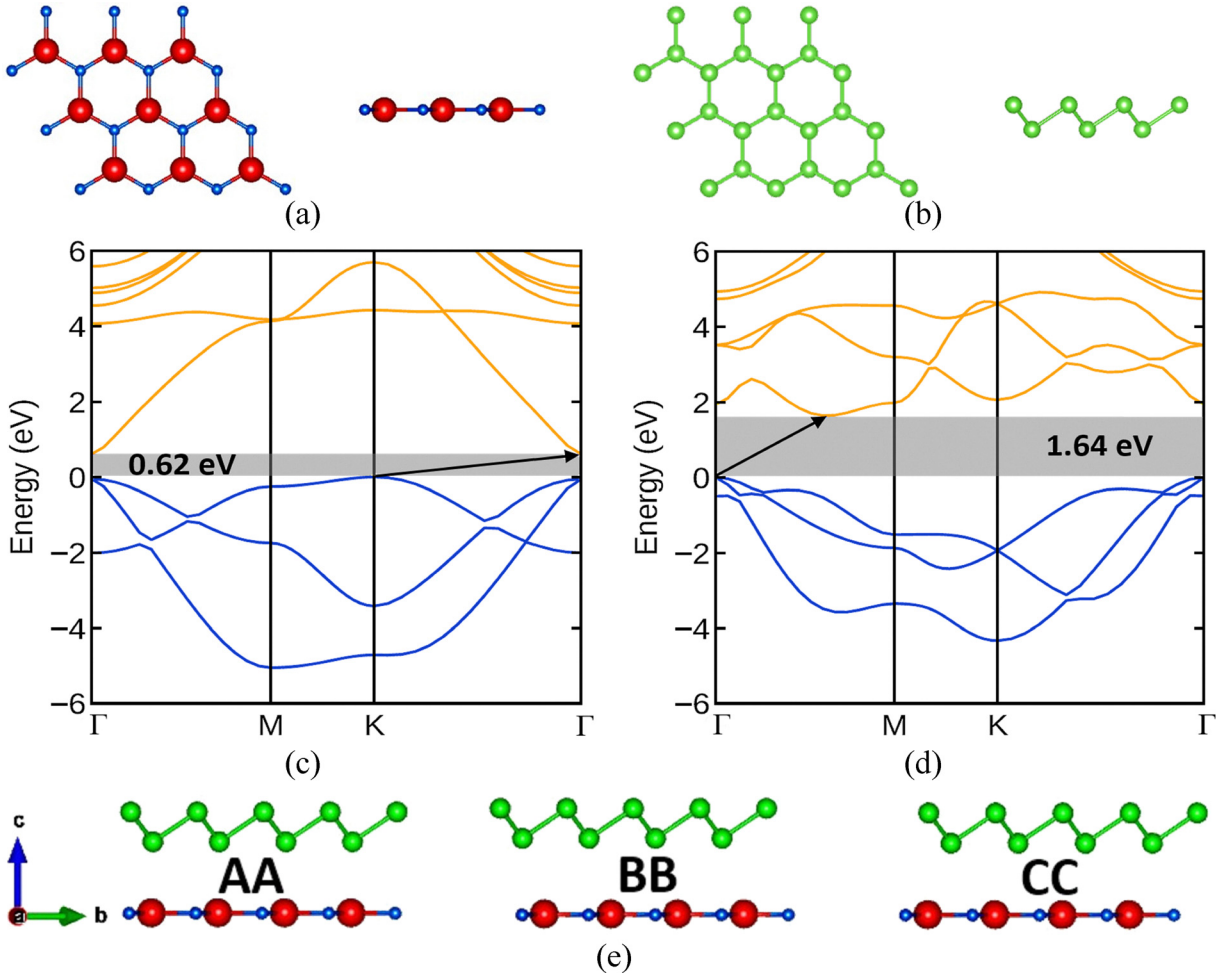

Fig. 1 Fully optimized atomic structures of (a) InN and (b) As monolayers as viewed from top and side positions. The PBE calculated band structures for (c) InN and (d) As monolayers. Diagrammatic representation of the (e) different stacking arrangements. Red, blue and green represent the In, N and As atoms, respectively.

As demonstrated in Fig. 1(e), three distinct stacking configurations were evaluated for the proposed heterostructure, labeled as AA (with As positioned above In), BB (with As positioned above N) and CC (with As positioned above the ring center) stackings. The binding energies for the AA, BB and CC stacking are −35.2, −27.5 and −34.1 meV Å^{-2}, respectively. The presence of a negative E_b suggests that the development of the heterostructure releases energy, indicating exothermicity. This leads to the thermodynamic stability of the InN/As heterostructure. Moreover, the E_b of all stackings is lower than −18 meV Å^{-2} measured for graphite, implying that the InNAs heterostructure is mostly held together by vdW interactions and experimentally synthesizable. E_b of AA stacking has been found to demonstrate the highest negative value, indicating its greater stability as a heterostructure. After identifying the most stable stacking configuration based on the E_b analysis, all subsequent electronic, optical and photovoltaic properties calculations were performed exclusively for the energetically favorable AA stacking.

The interlayer distance (d) between InN and As in the equilibrium AA geometry is 3.31 Å, which suggests the absence of chemical bonds and only weak vdW forces govern the interactions between the monolayers. The sum of covalent radii between In and N (1.42 + 1.19 = 2.61 Å) is much lower than d, further confirming no covalent bond formation in the hybrid interface. To further assess the thermal stability, we conducted AIMD using an NVT ensemble. These simulations were carried out at a temperature of 300 K with time steps of 6 ps. The plot in Fig. 2(b) suggests that following a 6 ps heating interval, there was very little change in the overall energy of the InN/As heterostructure and its atomic structure still retains a reasonable original morphology. Hence, the investigated heterostructure exhibits thermal stability at standard ambient temperature. The high thermodynamic stability strongly indicates that this heterostructure has the ability to remain intact at ambient temperature. The calculated elastic constants of C_{11} = 142 N m^{-1}, C_{22} = 143 N m^{-1}, C_{12} = 61 N m^{-1} and C_{66} = 41 N m^{-1} serve as a link connecting the mechanical properties of a material to the description of internal forces, such as stability and stiffness.[30] The mechanical stability of the investigated InN/As is confirmed based on the criteria $C_{11}C_{22} > 0$ and C_{11}, C_{22}, $C_{66} > 0$.[31]

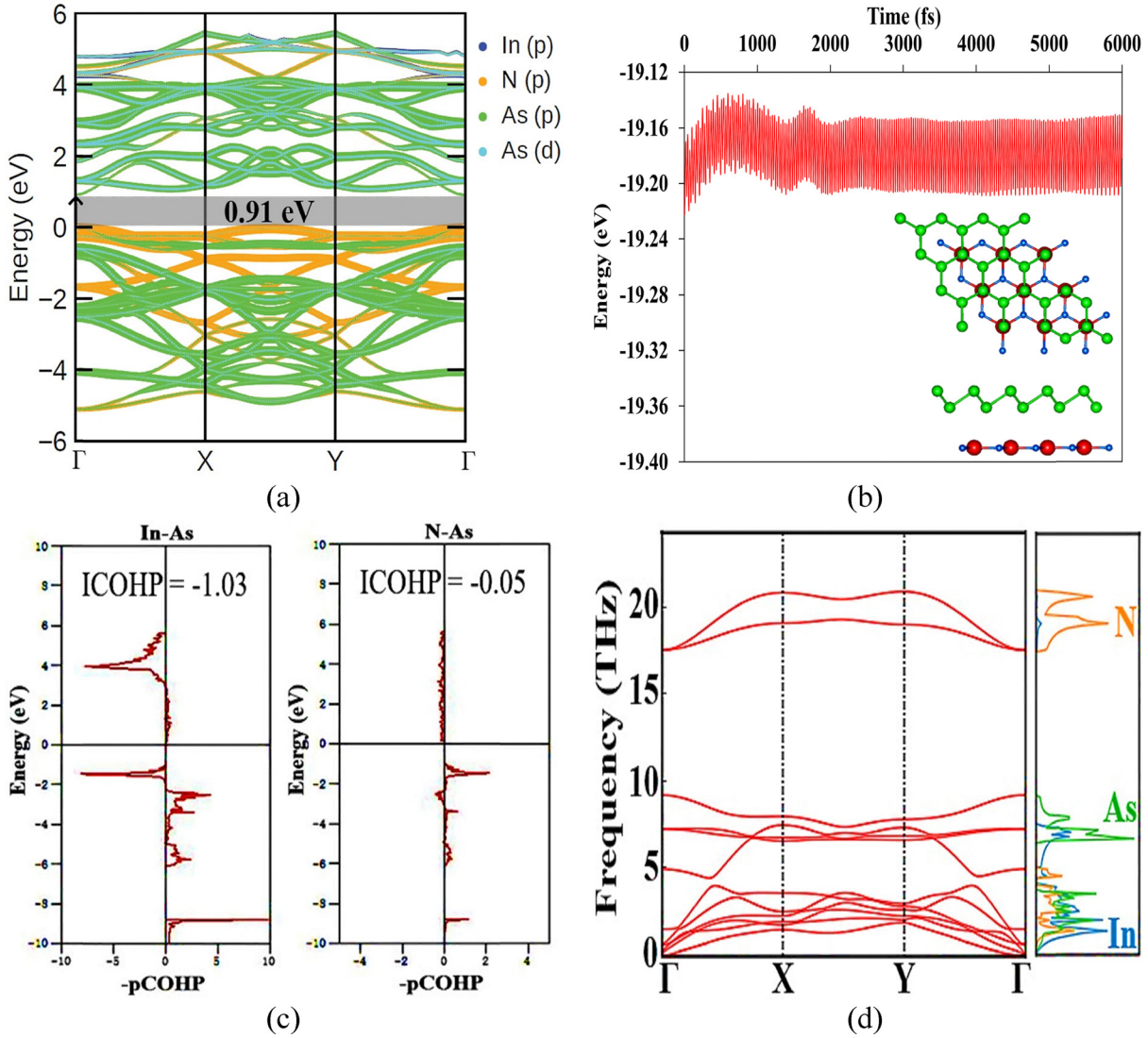

Fig. 2 (a) The PBE calculated band structure and (b) evolution of total energy for the InN/As heterostructure as simulated by AIMD at 300 K for 6 ps. The final configuration is shown in the inset for comparison. (c) −pCOHP for In–As and N–As interactions. (d) Phonon dispersion plot of the InN/As heterostructure. The E_F is marked by a horizontal solid black line at 0 eV.

Using the LOBSTER tool,[32] the bond strengths of In–As and N–As were additionally determined by conducting calculations of the projected and integrated crystal orbital Hamilton population (pCOHP and ICOHP), as depicted in Fig. 2(c). The −pCOHP diagram represents bonding and antibonding contributions as positive and negative values, respectively. The heterostructure has stable chemical bonding interactions due to the absence of antibonding states at the Fermi level (E_F). Furthermore, the bonding states contribute more than the antibonding states below the E_F, which aids in stabilizing the InN/As heterostructure. The primary contribution to the antibonding and bonding states near E_F in InN/As is mostly provided by N–As bonds. This observation is consistent with the electronic properties outcome. ICOHP is another important metric for evaluating the bond strength, in which a negative value signifies a strong bond. Both In–As and N–As have negative ICOHP. The phonon dispersion along the high-symmetry paths depicted in Fig. 2(d) reveals the absence of imaginary frequencies across all modes within the Brillouin zone, thereby confirming the dynamic stability of InN/As.

To provide a clearer understanding of how weak interactions impact the electronic structure of the nanomaterial, we performed calculations to determine the band structures of the InN/As heterostructure. Fig. 2(a) depicts the electronic band structure of the InNAs heterostructure. Unlike its separate components, the CBM and VBM of InN/As are located at the Γ point, signifying a direct 0.91 eV gap. The direct E_g of InN–As allows the electrons in the VB to be directly excited to the CB without the need for phonons. This process just requires the absorption of energy, which is a change in energy without any change in the position. As a result, the probability of emitting energy in the form of photons is higher. This characteristic makes them highly ideal for use in electroluminescent devices and optoelectronic devices. Together with the projected density

of states (PDOS) plot in S2 of the ESI,† these analyses clearly indicate that upon forming contact between InN and As monolayers, the CBM is dominated by p orbitals of As while the VBM is largely contributed by p orbitals of N, implying the formation of a staggered type-II heterostructure with an extremely narrow, near zero conduction band offset (CBO) of 4×10^{-3} eV that corresponds to less energy loss, shown in Fig. 3(a).

As shown in Fig. 3(b), the electrostatic potential of InN is far deeper than that of As. Translocation of electrons from InN to the As causes a positive charge to build up around the InN layer, while a negative charge builds up around the As layer. The E_F of InN and As decreases and increases at the same time, eventually reaching equilibrium and giving rise to a large potential drop of 11.9 eV. The large potential drop induces a built-in electric field at the interface of the heterostructure, which plays a crucial role in the separation of the photogenerated electron–hole pairs. Referring to the inset of Fig. 3(b), the regions where charges accumulate are indicated in yellow, while the regions where charges are depleted are shown in blue. The analysis provides additional evidence that aligns with Bader findings, revealing that electrons tend to gather near the As layer, resulting in a depletion of electrons in the InN layer. The redistribution of positive and negative charges creates an internal electric field at the interface, thereby preventing carrier recombination and extending the lifetime of optoelectronic devices, hence improving their performance. Bader charge-population analysis[33] indicates that the As layer acquired a charge of 0.017 |e| from the InN layer, further reflecting electron transport at the heterostructure interface. The work function (Φ) of InN and As monolayers was determined to be 4.84 and 5.42 eV, respectively. The lower value of Φ for InN again distinctly indicates that electron transport occurs from InN to As. This observation is consistent with the previously discussed findings on the electrostatic potential of the InN/As heterostructure.

3.2. Optoelectronic properties

To account for optical responses that go beyond the independent-particle approach, we calculated the frequency-dependent dielectric function by solving the BSE with a scissor shift to incorporate excitonic effects. The number of bands was five times greater than in the optimization stage. The $\alpha(\omega)$ curve of InNAs exhibits a red shift compared to the isolated As component, resulting in an increase in $\alpha(\omega)$ in the visible regions and significant capture of infrared photons. The absorption edge of the heterostructure occurs at around 0.8 eV, which closely aligns with its E_g.

As shown in Fig. 4(a) and (b), formation of the InNAs heterostructure not only broadens the range of light absorption, but also significantly enhances the intensity of absorption. InNAs exhibits a wide absorption spectrum, with $\alpha(\omega)$ reaching up to 5×10^5 cm^{-1} in the near ultraviolet (UV) range, up to 3.5×10^5 cm^{-1} in the visible range accompanied by more noticeable peaks and up to 5×10^4 cm^{-1} in the near infrared (NIR) range, confirming that heterostructures are more effective in utilizing light in the ultraviolet and visible regions compared to monolayers. These $\alpha(\omega)$ values even surpass those reported for other Janus group-III monochalcogenides such as MoSSe,[34] PtSSe[35] and GeTeI.[36] The increase in light absorption can be attributed to the charge transfer and interlayer coupling of the heterostructure, resulting in the overlapping of electronic states in the VB. This scenario has also been observed in earlier heterostructure works,[37,38] as well as in recent studies on advanced 2D semiconductor systems that highlight the critical role of interfacial interactions in modulating optical absorption and enhancing light–matter interactions.[39–45] Our results further confirm that heterostructure engineering provides an effective pathway for enhancing light absorption in 2D materials, making the InN/As system a promising candidate for future optoelectronic applications.

Maximizing μ is crucial for minimizing the detrimental recombination of photo-generated electron–hole pairs. This

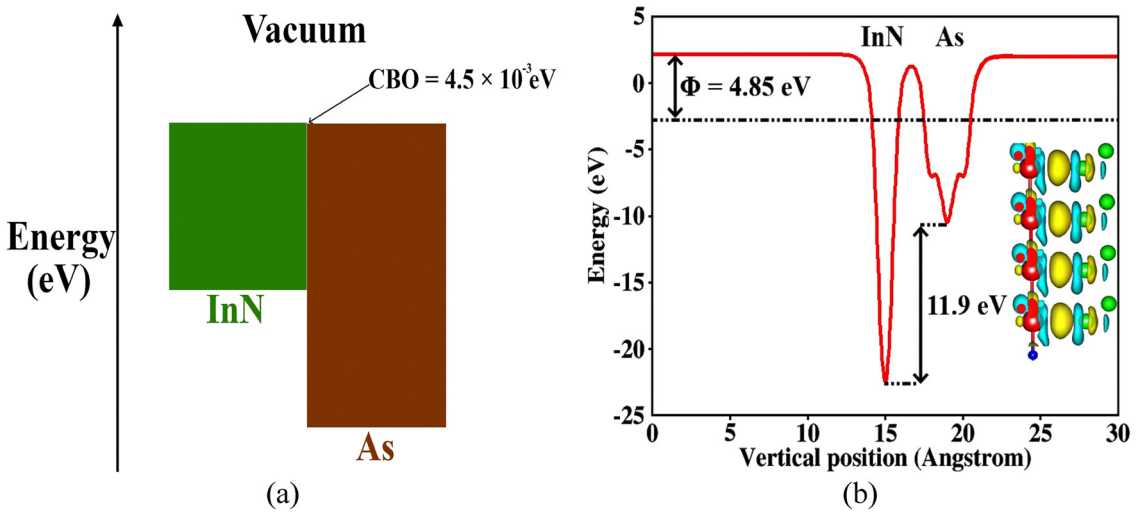

Fig. 3 Diagram illustrating the (a) band alignment and (b) average electrostatic potential along the z-direction of the type-II InN/As heterostructure, with the charge-density difference plot as the inset. The yellow area denotes the accumulation of charge, whilst the blue portion signifies the dispersal of charge. The isosurface value was set to 5×10^{-4} e Å^{-3}.

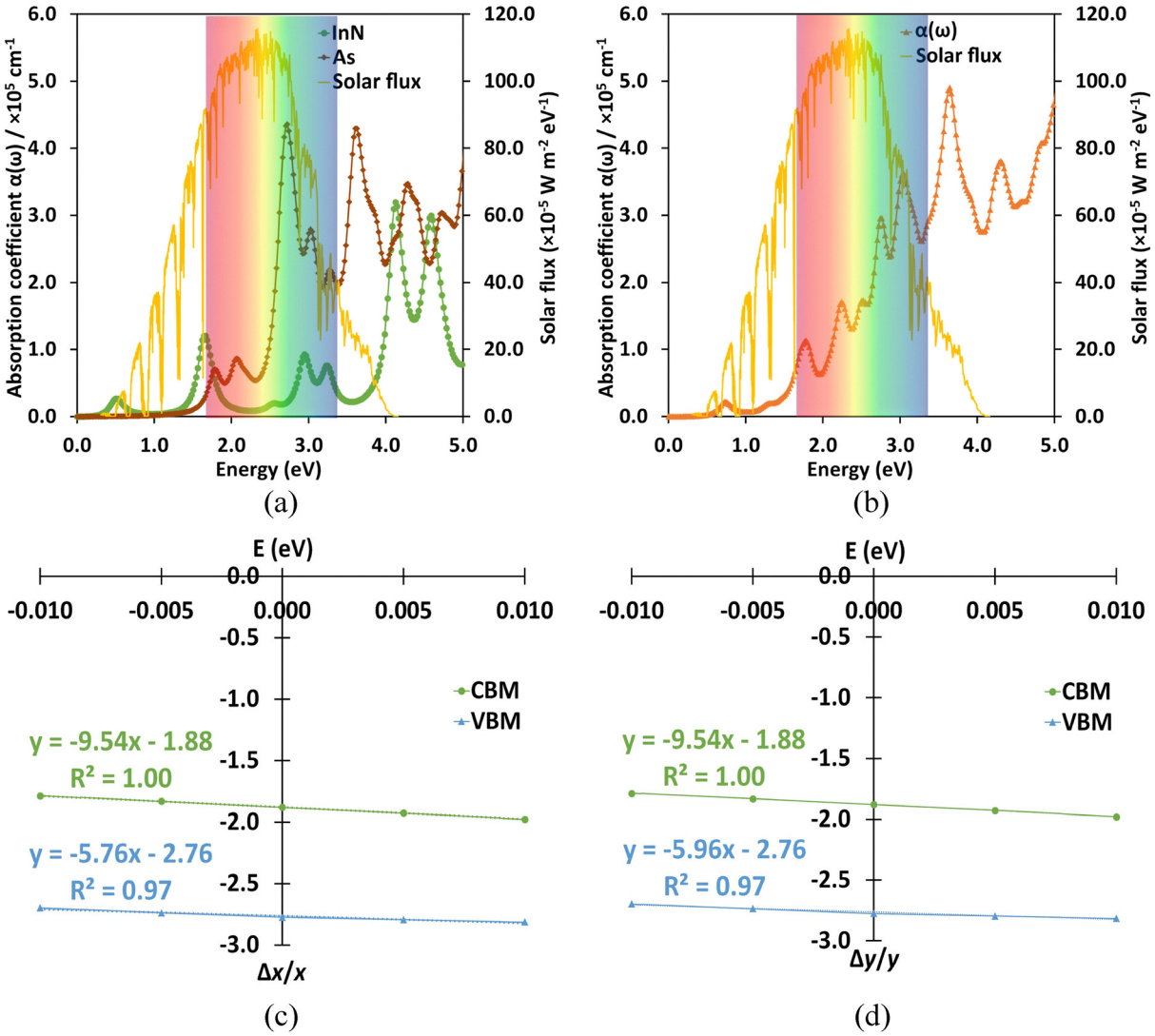

Fig. 4 Absorption coefficient $\alpha(\omega)$ for (a) InN and As monolayers and (b) InN/As heterostructure as a function of frequency. An adequate number of empty bands were included in the computations, set to be five times those of valence bands. Band edge energies as a function of strain in (c) *x* and (d) *y* directions for the InN/As heterostructure.

parameter is a measure of the velocity at which electrons and holes flow within a semiconductor. The μ of InNAs was determined by employing the phonon-limited scattering technique, utilizing the deformation potential theory[46] and the following expression.

$$\mu(2D) = \frac{eC_{2D}\hbar^3}{k_B T m^* m E_D^2} \quad (3)$$

where k_B, T, m^*, m, e, E_D, C_{2D} and $\hbar$ represent the Boltzmann constant, room temperature of 300 K, effective mass of the charge carrier along the transport direction, average effective mass along the two orthogonal directions, electron charge and deformation potential constant as indicated in the trendlines of Fig. 4(c) and (d), respectively. C_{2D} is the stretching modulus in the propagation direction calculated by $2(\partial^2 E_{total}/\partial l^2)/A$, where E_{total} is the total energy in response to the uniaxial strains ε. The average relative ratio ($D = m_e/m_h$) is a useful measure that reflects the recombination rate. Generally, when D is greater than one, it is linked to a slower recombination process. As shown in Table 1, the electron μ along zigzag and armchair directions exceed 867 $cm^2\ V^{-1}\ s^{-1}$, which are 6 times the hole carrier μ in the same directions and dramatically enhanced relative to those calculated for InN ($\sim$787 $cm^2\ V^{-1}\ s^{-1}$) and As

Table 1 Calculated effective mass m (m_o), E_D (eV), C_{2D} (N m^{-1}) and μ ($cm^2\ V^{-1}\ s^{-1}$) for holes and electrons in the direction of zigzag (*x*) and armchair (*y*) at 300 K. E_b^{ex} (eV) was calculated *via* $E_b^{ex} = 13.56(\mu/\varepsilon_0^2)$ where $\mu = (m_e^{-1} + m_h^{-1})$ and $\varepsilon_0 = 3.48$ denote the reduced effective mass and static dielectric constant, respectively

Direction	Carrier type	m	E_D	C_{2D}	μ	E_b^{ex}
Zigzag	Holes	0.847	5.76	171	153.35	0.19
	Electrons	0.215	9.54		867.68	
Armchair	Holes	0.844	5.96	171	143.68	
	Electrons	0.214	9.54		871.73	

($\sim$21 $cm^2\ V^{-1}\ s^{-1}$) monolayers.[47,48] Moreover, the average hole μ of $\sim$148 $cm^2\ V^{-1}\ s^{-1}$ in the InN/As heterostructure is significantly increased by nearly two orders of magnitude compared to that of the individual monolayers, 84 $cm^2\ V^{-1}\ s^{-1}$ and 66 $cm^2\ V^{-1}\ s^{-1}$ for InN and As, respectively, overcoming the inherent limitation of the monolayers with low μ.

Thus, the recombination of photogenerated carriers is reduced due to the disparity in the magnitudes of the μ of holes and electrons. The comparatively higher C_{2D} signifies a reduced quantity of phonons in the crystal and a decreased probability of electron–phonon scattering, which is advantageous for increasing the μ. In addition to its type-II characteristic, the spatial separation (3.31 Å) of photogenerated electron–hole pairs, intrinsic built-in electric field and the indirect E_g of individual InN and As monolayers can all work in tandem to slow down the energy-wasted recombination in the heterostructure. The exciton binding energy (E_b^{ex}) can be employed to compute the Coulombic force of interaction that binds the exciton. Exciton is a bound state that occurs when a pair of electrons and holes, which are produced by the absorption of light, are located together. Hence, the energy needed to disassemble an exciton into liberated charge carriers, namely electrons and holes, is referred to as E_b^{ex}. The computed E_b^{ex} value, listed in Table 1, was determined to be 0.19 eV, which meets the criterion for a solar cell with a low E_b^{ex} of approximately 0.13 eV.[49]

To assess the practical viability of the InN/As heterostructure for solar cell applications, the PCE was determined using Scharber's method,[50] given as

$$\eta_{PCE} = \frac{0.65\left(E_g^d - CBO - 0.3\right)\int_{E_g^d}^{\infty}\frac{P(\hbar\omega)}{\hbar\omega}d(\hbar\omega)}{\int_0^{\infty}P(\hbar\omega)d(\hbar\omega)} \quad (4)$$

where E_g^d and $P(\hbar\omega)$ are the E_g of InN as the donor and solar flux at the AM1.5 photon energy ($\hbar\omega$). The value of 0.3 eV serves as an empirical parameter to approximate the losses resulting from energy conversion kinetics. Typically, heterostructures with CBO $>$ 1.0 eV or donor E_g^d $<$ 0.5 or $>$3.0 eV are not anticipated to produce high PCE. As shown in Fig. 5(a), the upper-limit PCE for the InN/As heterostructure was determined to be 17.9%, showcasing a competitive edge in comparison to current 2D heterojunction solar cells, such as MoS_2/WSSe (9.4%),[51] InSe/Te (13.4%),[52] g-C_3N_4/GaAs (15.2%)[53] and Phosphorene/MoS_2 (17.5%),[54] concluding that it is a strong contender in the field of 2D heterostructure solar cells. The spectroscopic limited maximum efficiency (SLME) was additionally estimated using the method proposed by Yu *et al.*[55] for differentiating the performance between InN/As and its constituent components. The relevant equations and calculations can be found in S1 of the ESI.† This parameter represents the highest attainable efficiency of a solar cell, and is calculated by utilizing the E_g of the material under study and the $\alpha(\omega)$. Fig. 5(b) shows the thickness dependent SLME for InNAs and the constituent monolayers. Due to its narrow CBO and suitable E_g value, the SLME for the InN/As heterostructure was determined to be $\sim$28%, surpassing the values measured for InN ($\sim$18%) and As ($\sim$19%) monolayers, concluding that it is a strong contender in the field of 2D heterostructure solar cells.

While there are worries about the toxicity of As, its use in treating tumors has been documented.[56] The As nanosheets have been found to exhibit selective cytotoxicity towards cancer cells, resulting in an inhibition rate of 82%. In addition, the toxicity tests conducted on mice by delivering arsenic demonstrated the presence of typical blood cell indicators, as well as the absence of inflammation and infection in the kidneys and liver.[57] Wang *et al.*[58] have documented the biocompatibility of As nanosheets in combatting carcinogenic substances, highlighting the non-toxic dispersion of arsenic in the bloodstream.

3.3. Moisture effect on the optoelectronic performance

The optoelectronic properties of solar cells are widely recognized to be influenced by humidity during practical use. It is imperative to provide clarification on the impact of dampness on the delicate mechanism. From a theoretical standpoint,

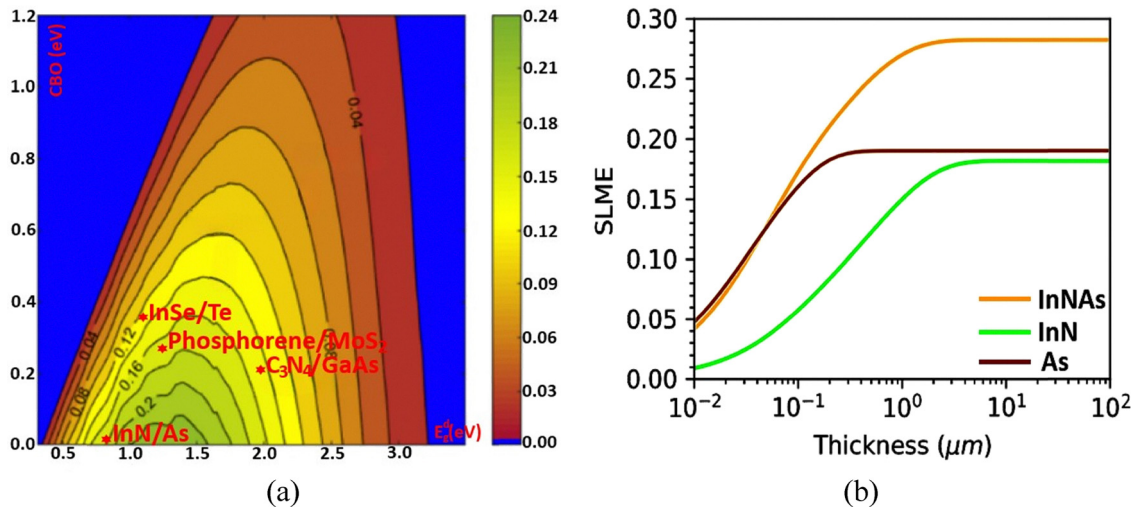

Fig. 5 (a) Calculated PCE contour as a function of the E_g^d and CBO. Heterostructure type is marked by red stars. (b) SLME (at 300 K) as a function of film thickness for the InNAs heterostructure and its constituent monolayers.

quantifying the humidity % in experiments is a challenge. Thus, the current conditions of relative humidity can be simulated by depositing water molecules onto the adsorbent surface. Due to InN acting as the substrate, water molecules are presumed to interact with the top As layer. Two configurations were evaluated, specifically As-top and hollow-top. The adsorption energy (E_{ads}) of the water molecule was determined by calculating the difference in energy between the total energy of the adsorbent with the adsorbed water molecule ($E_{complex}$), the energy of the adsorbent surface without the water molecule ($E_{surface}$) and the energy of the isolated water molecule (E_{water}), based on the relation

$$E_{ads} = E_{complex} - (E_{surface} + E_{water}) \quad (5)$$

E_{water} was estimated by simulating the isolated water molecule within a broken symmetry cell, using a lattice constant of 10 Å and employing the same settings as those stated for the surfaces. While the hollow-top configuration yields the lowest E_{ads} value, the measured E_{ads} of −0.028 eV is far below the 0.5 eV criterion for chemisorption[59,60] and the bond length between H and As atoms (2.41 Å) is much longer than the usual 1.52 Å for H–As, indicating a weak physisorption or nearly negligible interaction between them, resulting in only a minor red shift, thereby confirming that water molecules have a negligible effect on the energy band shape. The E_{ads} decreases further to −0.015 eV as water molecules are increased to two.

As revealed in Fig. 6(b), the E_g of InN/As remains direct type at Γ and increases marginally to 0.87 eV when more water molecules are adsorbed onto the surface of As atoms, with no noticeable changes around the E_F vicinity as the water concentration increases.

4. Conclusions

Both InN and As monolayers are experimentally proven, indirect E_g materials. For the first time, the stacking of these monolayers in an InN/As heterostructure was presented to thoroughly investigate its structural stability, electronic and optical properties using state-of-

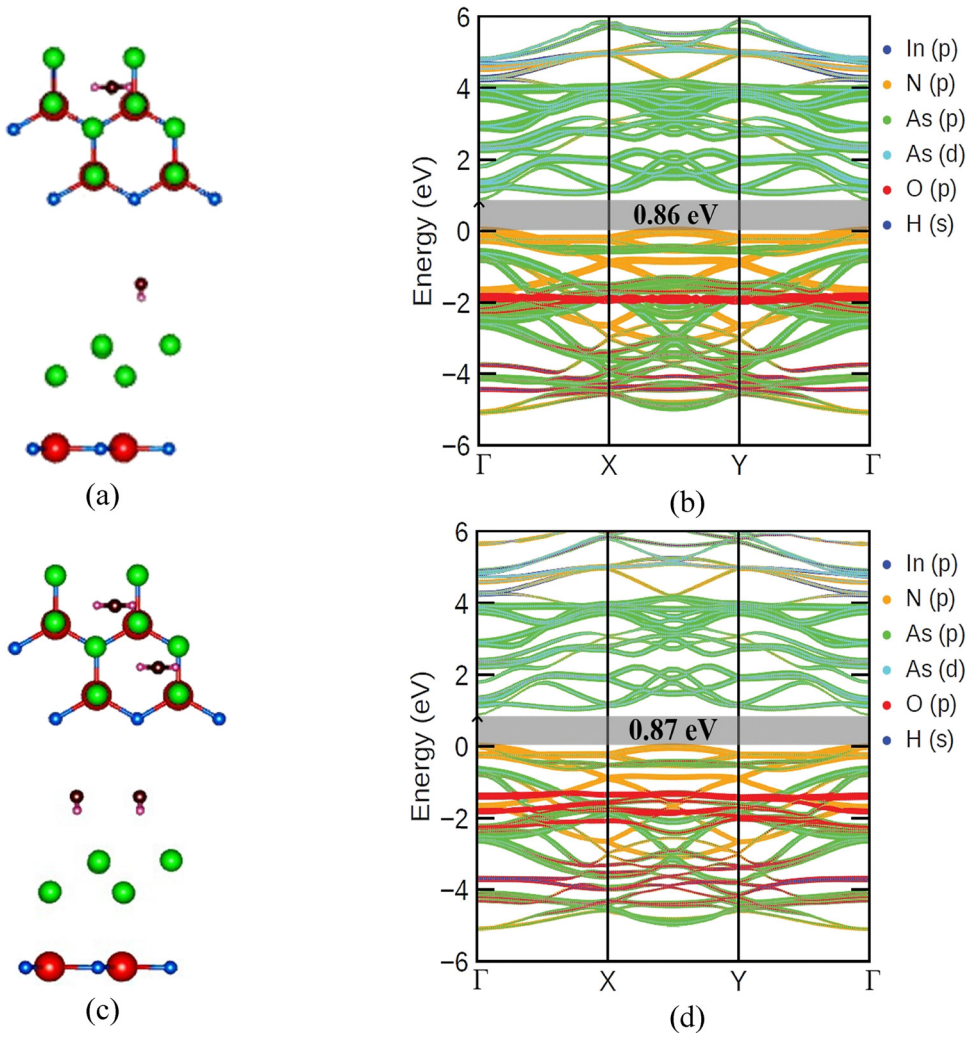

Fig. 6 (a) Optimized structure of water molecule adsorbed InN/As (top and side views) and its (b) calculated band structure. (c) Two water molecule adsorbed InN/As (top and side views) and its (d) calculated band structure. Brown and pink spheres denote the O and H atoms, respectively.

the-art first-principles calculations. The investigated structure has been determined to be energetically, thermally and mechanically stable. The discovered energy band structure reveals that InN/As is a direct E_g semiconductor, possessing favourable attributes such as high electron mobility and efficient absorption of IF to UV light compared to its constituent monolayers, rendering it more viable for use in optoelectronic applications. Its predicted PCE can attain a maximum value of 17.9%, placing it in direct competition with other 2D heterostructures that have been previously investigated. This study not only offers valuable instructions for creating new vdW heterostructures but also demonstrates that the stacking process is an effective strategy for converting materials with indirect E_g into direct E_g in the bilayer form.

Author contributions

Y. H. R. Chang: conceptualization, methodology, software, formal analysis, investigation, data curation, project administration, and writing – original draft. K. H. Yeoh and M. H. Tuh: software, formal analysis, investigation, validation, resources, and writing – review and editing. J. Jiang and Q. Liang: formal analysis, validation, resources, and writing – review and editing.

Conflicts of interest

There are no conflicts to declare.

Data availability

The authors confirm that the data supporting the findings of this study are available within the article and/or its ESI.†

References

1 A. Geim and K. Novoselov, The rise of graphene, *Nat. Mater.*, 2007, **6**, 183–191.
2 M. Krawiec, Functionalization of group-14 two-dimensional materials, *J. Phys.: Condens. Matter.*, 2018, **30**, 233003.
3 J. Zhao, Z. H. Qi, Y. Xu, J. Dai, X. C. Zeng, W. Guo and J. Ma, Theoretical studies on tunable electronic structures and potential applications of two-dimensional arsenene-based materials, *Wiley Interdiscip. Rev.: Comput. Mol. Sci.*, 2019, **9**(2), e1387.
4 J. Shah, W. Wang, H. M. Sohail and R. I. G. Uhrberg, Experimental evidence of monolayer arsenene: an exotic 2D semiconducting material, *2D Mater.*, 2020, **7**, 025013.
5 J. Wu, W. Walukiewicz, K. M. Yu, J. W. Ager, E. E. Haller, H. Lu, W. J. Schaff, Y. Saito and Y. Nanishi, Unusual properties of the fundamental band gap of InN, *Appl. Phys. Lett.*, 2002, **80**, 3967–3969.
6 K. Sugita, H. Takatsuka, A. Hashimoto and A. Yamamoto, Photoluminescence and optical absorption edge for MOVPE-grown InN, *Phys. Status Solidi B*, 2003, **240**, 421–424.
7 W. Meng, X. Wang, Z. Xiao, J. Wang, D. B. Mitzi and Y. Yan, Parity-forbidden transitions and their impact on the optical absorption properties of lead-free metal halide perovskites and double perovskites, *J. Phys. Chem. Lett.*, 2017, **8**, 2999–3007.
8 D. Jariwala, A. R. Davoyan, J. Wong and H. A. Atwater, van der Waals Materials for atomically thin photovoltaics: promise and outlook, *ACS Photonics*, 2017, **4**, 2962–2970.
9 A. Chaves, J. G. Azadani, H. Alsalman, D. R. da Costa, R. Frisenda, A. J. Chaves, S. H. Song, Y. D. Kim, D. He, J. Zhou, A. Castellanos-Gomez, F. M. Peeters, Z. Liu, C. L. Hinkle, S.-H. Oh, P. D. Ye, S. J. Koester, Y. H. Lee, P. Avouris, X. Wang and T. Low, *npj 2D Mater. Appl.*, 2020, **4**, 29.
10 Y. H. R. Chang, J. Jiang, K. H. Yeoh, H. Y. Khong, M. M. Mahat, S. S. Chai, I. Saad and M. H. Tuh, Improved thermoelectric-photovoltaic performance of Ag_2Se originating from a halogenation-induced wider band gap and low crystal symmetry, *ACS Appl. Energy Mater.*, 2022, **5**, 6019–6031.
11 Y. H. R. Chang, K. H. Yeoh, J. Jiang, S. S. Chai, Y. Z. Abdullahi, H. Y. Khong, T. L. Lim and M. H. Tuh, Forecasting the Unrevealed Surface-Controlled Photocatalytic Water Splitting in Two-Dimensional Ag_2Se with Ultrafast Carrier Mobility: A First-Principles Study, *Catal. Sci. Technol.*, 2023, **13**, 4813–4822.
12 T. T. Tran, J. R. Panella, J. R. Chamorro, J. R. Morey and T. M. McQueen, Designing indirect-direct bandgap transitions in double perovskites, *Mater. Horiz.*, 2017, **4**, 688–693.
13 T. Sun, Z. Ma, M. Yao, J. Wei, Y. Liu and X. Ming, Direct band-gap iodide double perovskite solar cell materials by doping strategy: First-principles predictions, *Mater. Today Commun.*, 2023, **37**, 107055.
14 H. Zeng, J. Zhao, A.-Q. Cheng, L. Zhang, Z. He and R.-S. Chen, Tuning electronic and optical properties of arsenene/C_3N van der Waals heterostructure by vertical strain and external electric field, *Nanotechnology*, 2018, **29**, 075201.
15 J. Zhao, Y. Qi, C. Yao and H. Zeng, Modulating the electronic properties and band alignments of the arsenene/$MoSi_2N_4$ van der Waals heterostructure via applying strain and electric field, *Phys. Chem. Chem. Phys.*, 2023, **25**, 33023–33030.
16 G. Kresse and J. Furthmüller, Efficient Iterative Schemes for *Ab initio* Total-energy Calculations Using a Plane-wave Basis Set, *Phys. Rev. B:Condens. Matter Mater. Phys.*, 1996, **54**, 11169–11186.
17 G. Kresse and J. Furthmüller, Efficiency of *Ab-initio* Total Energy Calculations for Metals and Semiconductors Using a Plane-wave Basis Set, *Comput. Mater. Sci.*, 1996, **6**, 15–50.
18 J. P. Perdew, K. Burke and M. Ernzerhof, Generalized gradient approximation made simple, *Phys. Rev. Lett.*, 1996, **77**, 3865–3868.
19 P. E. Blöchl, Projector Augmented-wave Method, *Phys. Rev. B:Condens. Matter Mater. Phys.*, 1994, **50**, 17953.
20 S. Grimme, S. Ehrlich and L. Goerigk, Effect of the damping function in dispersion corrected density functional theory, *J. Comput. Chem.*, 2011, **32**(7), 1456–1465.
21 J. Witte, N. Mardirossian, N. Neaton, J. B. Neaton and M. H. Gordon, Assessing DFT-D3 damping functions across widely used density functionals: can we do better, *J. Chem. Theory Comput.*, 2017, **13**, 2043–2052.
22 Y. H. R. Chang, J. Jiang, K. H. Yeoh, Y. Z. Abdullahi, H. Y. Khong, M. H. Tuh, F. K. Liew and Y. L. Liew, Achieving

type-II SnSSe/As van der Waals heterostructure with satisfactory oxygen tolerance for optoelectronic and photovoltaic applications, *J. Solid State Chem.*, 2023, **321**, 123925.

23 Y. H. R. Chang, K. Yao, K. H. Yeoh, M. Yoshiya, J. Jiang, M. H. Tuh, H. Y. Khong and T. L. Lim, Strain-Induced SiP-PtS_2 Heterostructure with Fast Carrier Transport for Boosted Photocatalytic Hydrogen Conversion, *J. Phys. Chem. C*, 2023, **127**(26), 12760–12769.

24 Y. H. R. Chang, K. H. Yeoh, J. Jiang, H. Y. Khong, M. M. Mahat, S. S. Chai, F. K. Liew and M. H. Tuh, Boosting the solar conversion efficiency of $MoSe_2/PtX_2$ (X = O, S) vdW heterostructure by strain and electric field engineering, *Phys. Scr.*, 2022, **97**, 115801.

25 K. H. Yeoh, K.-H. Chew, T. L. Yoon, Y. H. R. Chang and D. S. Ong, A first-principles study of two-dimensional $NbSe_2H$/g-ZnO van der Waals heterostructures as a water splitting photocatalyst, *Phys. Chem. Chem. Phys.*, 2021, **23**, 24222–24232.

26 Y. H. R. Chang, T. L. Yoon, T. L. Lim, P. W. Koh and M. H. Tuh, Frequency Dependent Linear and Nonlinear Optical Properties of Compositionally Tuned Inorganic CsSnX (X = Br, I) Composites, *J. Alloys Compd.*, 2019, **779**, 497–504.

27 Y. H. R. Chang, K. H. Yeoh, J. Jiang, T. L. Lim, Y. S. Yong, L. C. Low and M. H. Tuh, Constructing trifunctional $MoTe_2$/As van der Waals heterostructures for versatile energy applications, *New J. Chem.*, 2022, **46**, 20172–20181.

28 Y. H. R. Chang, T. L. Yoon and T. L. Lim, *Ab initio* Computations of The Linear and Nonlinear Optical Properties of Stable Compounds in Al-In-N System, *Curr. Appl. Phys.*, 2016, **16**(10), 1277–1283.

29 D. D. Vo, T. V. Vu, L. C. Nhan, C. V. Nguyen, H. V. Phuc, H. D. Tong, D. M. Hoat, L. T. Hoa and N. N. Hieu, Theoretical prediction of electronic and optical properties of haft-hydrogenated InN monolayers, *Superlattices Microstruct.*, 2020, **142**, 106519.

30 Y. H. R. Chang, T. L. Yoon, T. L. Lim and M. H. Tuh, High-pressure phases of $Al_xIn_{1-x}N$ compounds: First principles calculations, *J. Alloys Compd.*, 2017, **704**, 160–169.

31 S. Singh, L. Lang, V. Dovale-Farelo, U. Herath, P. Tavadze, F.-X. Coudert and A. H. Romero, MechElastic: A Python library for analysis of mechanical and elastic properties of bulk and 2D materials, *Comput. Phys. Commun.*, 2021, **267**, 108068.

32 S. Maintz, V. L. Deringer, A. L. Tchougreeff and R. Dronskowski, LOBSTER: A Tool to Extract Chemical Bonding from Plane-wave Based DFT, *J. Comput. Chem.*, 2016, **37**, 1030–1035.

33 W. Tang, E. Sanville and G. Henkelman, A grid-based Bader analysis algorithm without lattice bias, *J. Phys.: Condens. Matter*, 2009, **21**, 084204.

34 X. Ma, X. Wu, H. Wang and Y. Wang, A Janus MoSSe monolayer: a potential wide solar spectrum water-splitting photocatalyst with a low carrier recombination rate, *J. Mater. Chem. A*, 2018, **6**, 2295–2301.

35 R. Peng, Y. Ma, B. Huang and Y. Dai, Two-dimensional Janus PtSSe for photocatalytic water splitting under the visible or infrared light, *J. Mater. Chem. A*, 2019, **7**, 603–610.

36 N. Ghobadi, A. Rezavand, S. Soleimani-Amiri and S. G. Rudi, Surface-functionalization induced spintronic and photocatalytic features in group-III monochalcogenide monolayers: a first-principles study, *Appl. Surf. Sci.*, 2023, **639**, 158278.

37 X. Xu, L. Yang, Q. Gao, X. Jiang, D. Li, B. Cui and D. Liu, Type-II $MoSi_2N_4/MoS_2$ van der Waals Heterostructure with Excellent Optoelectronic Performance and Tunable Electronic Properties, *J. Phys. Chem. C*, 2023, **127**, 7878–7886.

38 N. B. Singh, R. Mondal, J. Deb, D. Paul and U. Sarkar, Density Functional Theory Studies of van der Waals Heterostructures Comprised of $MoSi_2P4$ and BAs Monolayers for Solar Cell Applications, *ACS Appl. Nano Mater.*, 2024, **7**, 6704–6711.

39 Y. Shen, X. Zhao, Z. Cui, K. Qin, D. Ma, F. Cheng, P. Yuan, X. Qi and E. Li, van der Waals ZnO/$HfSn_2N_4$ Heterojunction with Exceptional Photoresponse for Photodetectors, *ACS Appl. Mater. Interfaces*, 2024, **16**(43), 58802–58810.

40 Y. Shen, X. Zhao, Z. Cui, K. Qin, D. Ma, F. Cheng, P. Yuan, X. Qi and E. Li, First-principles investigation of the ZnO/$TiSn_2N_4$ heterojunction: A promising photoresponse material for high-performance photodetectors, *Appl. Surf. Sci.*, 2025, **687**, 162193.

41 Y. Shen, X. Zhao, Z. Cui, K. Qin, D. Ma, F. Cheng, P. Yuan, X. Qi and E. Li, g-ZnO/$HfGe_2N_4$ heterojunction: A novel semiconductor for efficient photocatalysis and optoelectronic detector applications, *Sol. Energy*, 2025, **297**, 113641.

42 Y. Shen, P. Yuan, Z. Yuan, Z. Cui, D. Ma, F. Cheng, K. Qin, H. Wang and E. Li, Modulation of electronic and optical properties of g-CN/XTe_2 (X= W, Mo) heterojunctions by biaxial strain, *Int. J. Hydrogen Energy*, 2024, **80**, 289–297.

43 Z. Cui, H. Wang, Y. Luo, E. Li, Y. Shen, K. Qin and P. Yuan, Mxenes/WSSe heterojunction photodetector with ultrahigh sensitivity and accuracy, *Appl. Surf. Sci.*, 2025, **684**, 161853.

44 Z. Cui, H. Meng, C. Zhang, L. Zhang, S. Zhang and L. Wang, MoSSe/Si_9C_{15} heterojunction photodetectors with ultrahigh photocurrent and carrier mobility, *Mater. Sci. Semicond. Process.*, 2024, **182**, 108705.

45 Y. Shen, P. Yuan, Z. Yuan, Z. Cui, D. Ma, F. Cheng, K. Yang, Y. Dong and E. Li, The electronic and optical properties of non-metallic doped g-C_3N_4/MoS_2 heterojunction, *Phys. Rev. B*, 2024, **674**, 415583.

46 J. Bardeen and W. Shockley, Deformation Potentials and Mobilities in Non-Polar Crystals, *Phys. Rev.*, 1950, **80**(1), 72–80.

47 C. Li, H. Liang, Z. Xu, J. Tao, Y. Zhang, K. Dong, L.-L. Wang and L. Xu, Construction of Z-scheme InN/BTe heterostructure for enhanced photocatalytic hydrogen evolution: DFT calculation and mechanism study, *Int. J. Hydrogen Energy*, 2024, **68**, 289–296.

48 Y. Wang, P. Huang, M. Ye, R. Quhe, Y. Pan, H. Zhang, H. Zhong, J. Shi and J. Lu, Many-body Effect, Carrier Mobility, and Device Performance of Hexagonal Arsenene and Antimonene, *Chem. Mater.*, 2017, **29**, 2191–2201.

49 A. Omirzak, Y. Wang, X. Ma and Z. Li, First-principles investigation of photovoltaic material based on lanthanide metals, *Comput. Mater. Sci.*, 2024, **233**, 112773.

50 M. C. Scharber, D. Mühlbacher, M. Koppe, P. Denk, C. Waldauf, A. J. Heeger and C. J. Brabec, Design rules for donors in bulk heterojunction solar cells - Towards 10% energy conversion efficiency, *Adv. Mater.*, 2006, **18**, 789–794.
51 B. T. Beshir, K. O. Obodo and G. A. Asres, Janus transition metal dichalcogenides in combination with MoS_2 for high-efficiency photovoltaic applications: a DFT study, *RSC Adv.*, 2022, **12**, 13749–13755.
52 Z. Ma, R. Li, R. Xiong, Y. Zhang, C. Xu, C. Wen and B. Sa, InSe/Te van der Waals Heterostructure as a High-Efficiency Solar Cell from Computational Screening, *Materials*, 2021, **14**, 3768.
53 J. Zhao, L. Han, B. Jia, H. Zhang, H. Zhao, J. Gao, J. Hao and P. Lu, Design of van der Waals heterostructures composed of g-C_3N_4 and III-V materials for solar cell, *Surf. Interfaces*, 2024, **50**, 104425.
54 J. Dai and X. C. Zeng, Bilayer phosphorene: Effect of stacking order on bandgap and its potential applications in thin-film solar cells, *J. Phys. Chem. Lett.*, 2014, **5**, 1289–1293.
55 L. Yu and A. Zunger, Identification of Potential Photovoltaic Absorbers Based on First-Principles Spectroscopic Screening of Materials, *Phys. Rev. Lett.*, 2012, **108**, 068701.
56 X. W. Zhang, X. J. Yan, Z. R. Zhou, F. F. Yang, Z. Y. Wu, H. B. Sun, W. X. Liang, A. X. Song, V. Lallemand-Breitenbach, M. Jeanne, Q. Y. Zhang, H. Y. Yang, Q. H. Huang, G. B. Zhou, J. H. Tong, Y. Zhang, J. H. Wu, H. Y. Hu, H. de The, S. J. Chen and Z. Chen, Arsenic Trioxide Controls the Fate of the PML-RAR Oncoprotein by Directly Binding PML, *Science*, 2010, **328**, 240–243.
57 J. Pei, J. Yang, T. Yildirim, H. Zhang and Y. Lu, Many-Body Complexes in 2D Semiconductors, *Adv. Mater.*, 2018, **31**, 1706945.
58 X. Wang, Y. Hu, J. Mo, J. Zhang, Z. Wang, W. Wei, H. Li, Y. Xu, J. Ma, J. Zhao, Z. Jin and Z. Guo, Arsenene: A Potential Therapeutic Agent for Acute Promyelocytic Leukaemia Cells by Acting on Nuclear Proteins, *Angew. Chem., Int. Ed.*, 2020, **59**, 5151–5158.
59 Y. H. R. Chang, Y. Z. Abdullahi, M. H. Tuh and T. L. Lim, Ultraviolet enhanced inorganic graphenylene-like $ZnMgX_2$ (X = O, S) for sensitive and reversible detection of toxic formaldehyde at room temperature: A first-principles study, *Surf. Interfaces*, 2024, **44**, 103722.
60 Y. H. R. Chang, Y. Z. Abdullahi, M. H. Tuh and K. H. Yeoh, Unveiling the adsorption, activation and reduction of CO_2 via inorganic, biphenylene akin Pt-doped $ZnMgO_2$, *Inorg. Chem. Commun.*, 2024, **162**, 112244.

